Unraveling the atomic and electronic structure of nanocrystals on superconducting Nb(110): Impact of the oxygen monolayer

Samuel Berman [1,*], Ainur Zhussupbekova [1,2], Brian Walls [1], Killian Walshe,[1] Sergei I. Bozhko,[3] Andrei Ionov,[3] David D. O'Regan,[1] Igor V. Shvets,[1] and Kuanysh Zhussupbekov [1,2,†]

[1]*School of Physics and Centre for Research on Adaptive Nanostructures and Nanodevices (CRANN), Trinity College Dublin, The University of Dublin, Dublin 2, D02 PN40, Ireland*
[2]*School of Chemistry, Trinity College Dublin, The University of Dublin, Dublin 2, D02 PN40, Ireland*
[3]*Institute of Solid State Physics, Russian Academy of Sciences, Chernogolovka, Russia*

The niobium surface is almost always covered by a native oxide layer which greatly influences the performance of superconducting devices. Here we investigate the highly stable niobium oxide overlayer of Nb(110), which is characterized by its distinctive nanocrystal structure as observed by scanning tunneling microscopy (STM). Our *ab initio* density functional theory (DFT) calculations show that a subtle reconstruction in the surface niobium atoms gives rise to rows of fourfold coordinated oxygen separated by regions of threefold coordinated oxygen. The fourfold oxygen rows are determined to be the source of the nanocrystal pattern observed in STM and the two chemical states of oxygen observed in core-level x-ray photoelectron spectroscopy (XPS) are ascribed to the threefold and fourfold oxygens. Furthermore, we find excellent agreement between the DFT calculated electronic structure with scanning tunneling spectroscopy and valence XPS measurements.

I. INTRODUCTION

Superconducting electronics are a cornerstone of modern science and technology, from superconducting radio-frequency cavities (SRFs) in particle accelerators [1–3], to qubits in quantum computers [4,5]. Niobium has emerged as one of the most attractive materials for superconducting electronics due to its high transition temperature and critical field [6], as well as its ease of fabrication [7]. Niobium samples typically contain a large amount of interstitial oxygen and quickly form an oxide layer when exposed to atmosphere [8,9]. While the superconducting gap of niobium is sensitive only to the presence of bulk interstitial oxygen [10–13], device properties such as coherence time in Josephson junctions [14,15], qubit relaxation time [16], and quality factor in SRF cavities [7,17–21] are greatly affected by the precise nature of the surface oxide layer. For SRF cavities, it has been shown that annealing the sample in ultrahigh vacuum conditions can compensate for the "Q drop" [22], i.e., the sharp drop of in quality factor (Q factor) above 80 mT [22,23]. The Q drop is believed to be a surface effect, with proposed mechanisms including local joule heating of inhomogeneities with high surface impedance [24] or the motion of magnetic vortices pinned at the surface [25]. Understanding the precise structure of the surface oxides is therefore vital for improving device performance.

The (110) surface of niobium has been studied by a variety of experimental techniques, including scanning tunneling microscopy/spectroscopy (STM/STS) [26–29],

low-energy electron diffraction (LEED) [26,30], grazing incidence x-ray diffraction (GIXRD) [8,31], Auger electron spectroscopy (AES) [9,28], and x-ray photoelectron spectroscopy (XPS) [26,32,33]. When exposed to atmosphere, a layered oxide structure of NbO, NbO_2, and amorphous Nb_2O_5 [31] is formed. The NbO_2 and Nb_2O_5 layers can be removed by annealing in ultrahigh vacuum (UHV), leaving only the NbO layer [8]. The remaining oxide is very difficult to remove, requiring annealing with temperatures close to the melting point of niobium, in excess of 2400 °C [11,34–37]. This structure will of course greatly influence the electronic structure of the surface, as well as the structure of additional layers formed on top of the surface [26]. Our STM experiments on this surface show a distinctive pattern of finite rows of wide protrusions, consistent with previous reports [26–28]. These rows of protrusions are termed the "nanocrystals," separated by disordered regions dubbed "channels" [see Fig. 1(a)].

Despite the technological and scientific relevance of the oxidized Nb(110) surface, very few calculations have been performed to understand its structure. While some previous works have performed calculations for the clean Nb(110) surface [34,38], the oxidized surface has received sparse attention. Kilimis *et al.* [39] performed DFT calculations studying the effect of twofold coordinated oxygen covering the surface, with a view towards understanding the early stages of the oxidation process. Other works have computed the minimum energy paths for diffusing oxygen atoms through the surface [40,41]. However, no previous reports have tackled the equilibrium structure or electronic properties of the nanocrystals, which plays a vital role in device performance. In this work, we investigate this surface structure by *ab initio* density functional theory (DFT) calculations, along with complementary
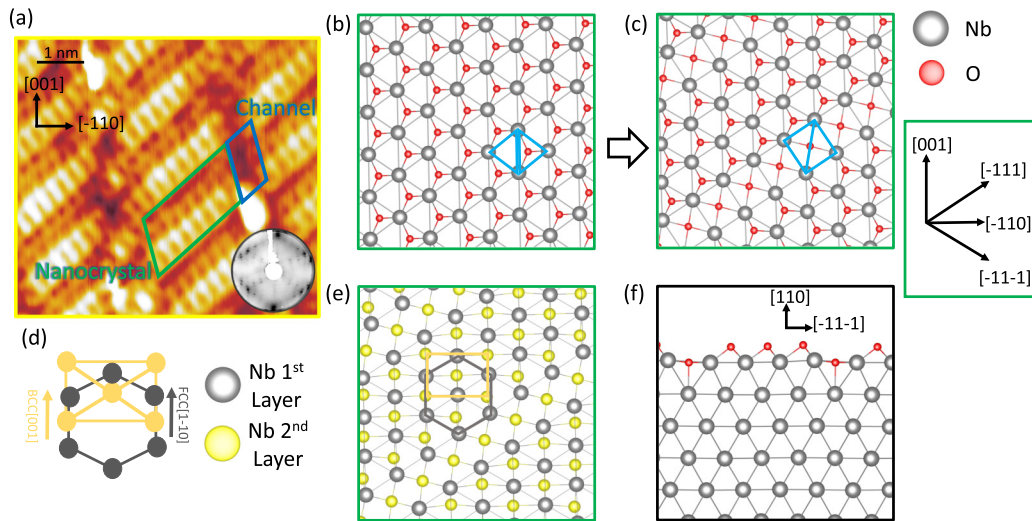
*bermans@tcd.ie
†zhussupk@tcd.ie

FIG. 1. (a) STM image of the surface with $V = 2$ mV, $I = 60$ pA, showing the nanocrystal and channel regions of the surface (with measured LEED pattern inset). (b) Unrelaxed and (c) relaxed structures of a full monolayer of oxygen, showing the emergence of a fourfold site (top view). (d) Schematic of the NW epitaxial relationship predicted from LEED experiments. (e) Top view of first and second Nb layers with oxygen removed to highlight the fcc-bcc epitaxial relationship. (f) Side view of relaxed geometry.

STM, STS, LEED, XPS, and UPS experiments. We show that this surface structure can be explained by a subtle oxygen induced reconstruction, with no need for niobium adatoms. In the Supplemental Material [42] (see also Refs. [43–45] therein) we show a similar analysis for models previously presented in the literature from Razinkin *et al.* [27] and Arfouai *et al.* [46], and demonstrate that these types of model cannot correctly explain the experimental data.

II. METHODS

A. Computational details

DFT calculations were carried out utilizing the QUANTUM ESPRESSO plane-wave self-consistent field (PWscf) package [47,48]. Throughout, the non-spin-polarized PBE exchange-correlation functional [49] and projector augmented wave (PAW) pseudopotentials [50] were used. We utilize symmetric Nb(110) slabs with nine atomic layers and vacuum padding of at least 10 Å, along with a wave function cutoff energy of 45 Ry, k-point sampling of $16 \times 16 \times 1$ in the Nb[-111], Nb[$-11-1$], and Nb[110] directions, respectively, and Marzari-Vanderbilt smearing [51] of 0.005 Ry giving a total energy convergence of <1 meV/atom. The number of k points was scaled when constructing the surface reconstruction according to the unit cell dimensions. Crystal structures were visualized in VESTA [52]. Simulated STM images and STS curves were obtained within the Tersoff-Hamann approximation [53,54], by integrating the local density of states (LDOS) over a small 0.037 Å^3 volume at a position of 4 Å above the surface [34,55,56]. Changes in binding energy are calculated by comparing the value of the electric potential at the atomic centers as in Refs. [57,58]. The work function was calculated by comparing the electric potential in the vacuum region ϕ_{vac} of the slab with the Fermi level E_f as in Ref. [59].

B. Experimental details

All experiments were performed *in situ* on the same (110) terminated niobium single crystal. The crystal was annealed at 850 °C under ultra-high-vacuum (UHV) conditions. During annealing the sample temperature was measured from a K-type thermocouple up to 600 °C, with temperatures above 600 °C estimated via an infrared optical pyrometer ($\epsilon = 0.25$). The crystal was transferred between two UHV systems via a UHV suitcase with a base pressure of low 10^{-10} mbar. All STM images demonstrated were obtained with a commercial Createc slider-type STM in constant-current mode at 77 K. The STM tips utilized were [001]-oriented single-crystalline W, which were electrochemically etched in NaOH. The bias was applied to the sample with respect to the tip. The UPS spectra were obtained with an excitation energy of He I (21.2 eV). XPS measurements were performed on an Omicron MultiProbe XPS system using monochromated Al K_α x rays (XM 1000, 1486.7 eV) with an instrumental resolution of 0.6 eV.

III. RESULTS

A. Crystal structure

To arrive at this model, we first consider a single isolated oxygen atom on top of the niobium surface. Several absorption sites are examined and our calculations confer with that of Tafen *et al.* [41], i.e., the oxygen atom sits in a threefold site on the surface. One might then expect that, for a full monolayer of oxygen on top of the surface, the oxygen would simply fill the threefold sites as in Fig. 1(b). However, when a full monolayer of oxygen is added we see a reconstruction take place, with the surface niobium atoms shifting to open up fourfold sites on part of the surface. The relaxation of this structure is shown in Figs. 1(b) and 1(c) and is accompanied by an energy drop of 0.11 eV/atom. The only choice that we make when constructing this model is the size and shape
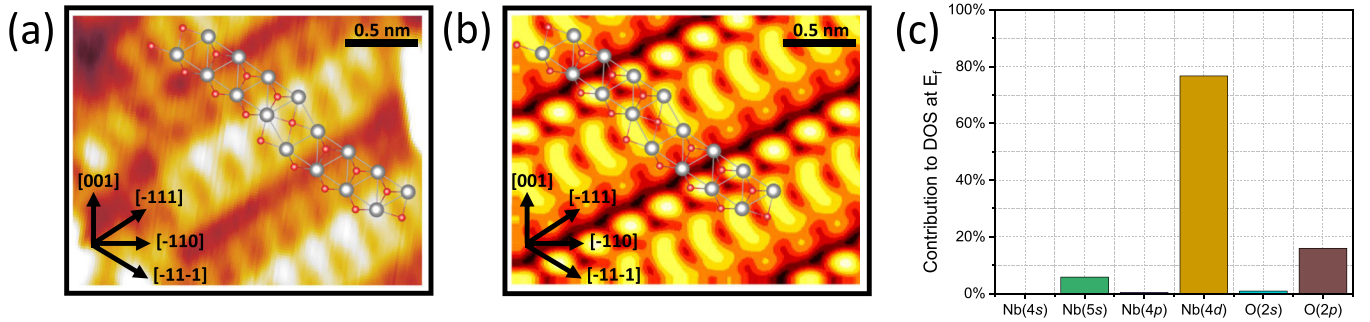
FIG. 2. Comparison between experimental and simulated STM. (a) Experimental STM image at bias 2 mV with suggested atomic structure superimposed. (b) Simulated STM image at a bias of 2 mV for the oxygen monolayer model with superimposed atomic structure. (c) Relative contribution of surface atom orbitals to the DOS at the Fermi level.

of the supercell in which the structure is allowed to relax. We simply choose a supercell which matches the periodicity observed in the experimental STM images [see Fig. 1(a) and Fig. 2(a)] (i.e., four unit cells along bcc[−11 − 1]). Initially, we consider an "infinite" nanocrystal as shown in Fig. 1(c), where the pattern extends infinitely along the bcc[−111] direction and the disordered channels are not included. This is sufficient for the purposes of calculating the local properties of the nanocrystals such as STM images and STS curves. However, we do also perform calculations with finite nanocrystals (full unit cell including channels), which are necessary for calculating global electronic properties for comparison with area averaged techniques such as XPS.

As shown in the top down crystal structure [Figs. 1(c) and 1(e)], the oxygen monolayer model displays a transition to the fcc (111) symmetry in the regions where the oxygen is threefold coordinated at the surface. In our calculations the epitaxial relationship closely resembles the Nishiyama-Wasserman (NW) orientation [(fcc)[1 − 10]||(bcc)[001]] observed in most experiments [8,26]. This is in agreement with the experimentally measured LEED pattern, shown in the inset of Fig. 1(a). Regarding the finite nature of the nanocrystals, previous STM studies have determined the average length of a nanocrystal to be between roughly 3.0 nm [9,27] and 3.5 nm [28]. Since this model still contains areas with fcc (111) symmetry, the previously proposed explanation for this behavior based on rigid lattice theory [27,28] still holds. Along the nanocrystals (fcc [110]/bcc [−111]) the mismatch is roughly $\simeq$4–5% between the lattices ($a_{fcc} = 2.98$ Å and $\frac{\sqrt{3}}{2}a_{bcc} = 2.86$ Å), meaning after roughly $\simeq$10–12 unit cells the two lattices will be out of phase. This causes the finite rows with roughly 10–12 protrusions each, with a total length of 3.0–3.5 nm.

B. Local electronic structure

Figures 2(a) and 2(b) show an experimental STM image of the nanocrystal structure, as compared to the simulated STM image from the reconstructed oxygen monolayer model at the same bias (2 mV). In the simulated image we can see that the distinctive rows of wide protrusions are present, with the area in between these rows comparing favorably also. Since the "monolayer of oxygen" model does not include any extra adatoms or major height variation on the surface, it is interesting to consider the origins of the protrusions observed in

STM. By considering the overlayed surface atomic structure on the simulated STM image in Fig. 2(b) we can see that the protrusions arise from the reconstructed fourfold area of the surface. This can be understood looking at the calculated superimposed atomic structure. In these reconstructed fourfold areas, the oxygen atoms sink deeper into the surface [see side view in Fig. 1(f)], leaving the niobium atoms in this area more exposed to the vacuum. In the unreconstructed areas with threefold oxygen, the oxygen sits on top of the niobium, passivating the niobium orbitals that protrude from the surface, and reducing the LDOS at the Fermi level. Since almost all of the density near the Fermi level comes from the niobium 4d states [Fig. 2(c)], it is reasonable that the areas of the surface with the niobium more exposed to the vacuum would show a higher LDOS around the Fermi level. The distinctive "wide" shape of the protrusions clearly arises from the fourfold square nature of the reconstructed area.

Turning to the STS, in Fig. 3(a) we can see good agreement between the experimentally measured STS and the LDOS as calculated in the vacuum above the slab for bias in the region −1 V to +2 V. In this region we observe minimal difference in the experimental STS on vs between the nanocrystal, and this is reflected also in the DFT simulation. The theoretical STS captures the relatively flat behavior around the Fermi level from −0.5 to 0.5 eV and the sharp increase above 0.5 eV. We see no evidence of resonances arising from surface states in the STS, such as was observed by Odobesko *et al.* [34] for the clean Nb(110) surface. Our results for this oxygen saturated surface align with their findings that this feature is suppressed in oxygen rich areas, confirming that the resonance is unique to the clean Nb(110) surface. The agreement between the theoretical and measured STS breaks down only at large negative bias (below −1 V), where we see a resonance at −1.5 V in the theory, which is most pronounced on the nanocrystal. This lack of agreement below −1 V has been observed for the clean Nb(110) surface as well by Odobesko *et al.* [34] and is not unexpected as tip states tend to dominate the tunneling matrix elements in this regime [34,60,61].

In order to better understand the nature of the electronic states at this surface we plot the m_l projected surface band structure [Fig. 3(b)]. In the case of the nanocrystal structure, there are two equivalent N points [along the nanocrystal (N_1) vs across the nanocrystal (N_2)]. We see clearly the absence of the z^2 surface state observed by Odobesko *et al.* [34] for the clean surface. Instead, the surface states below the Fermi level
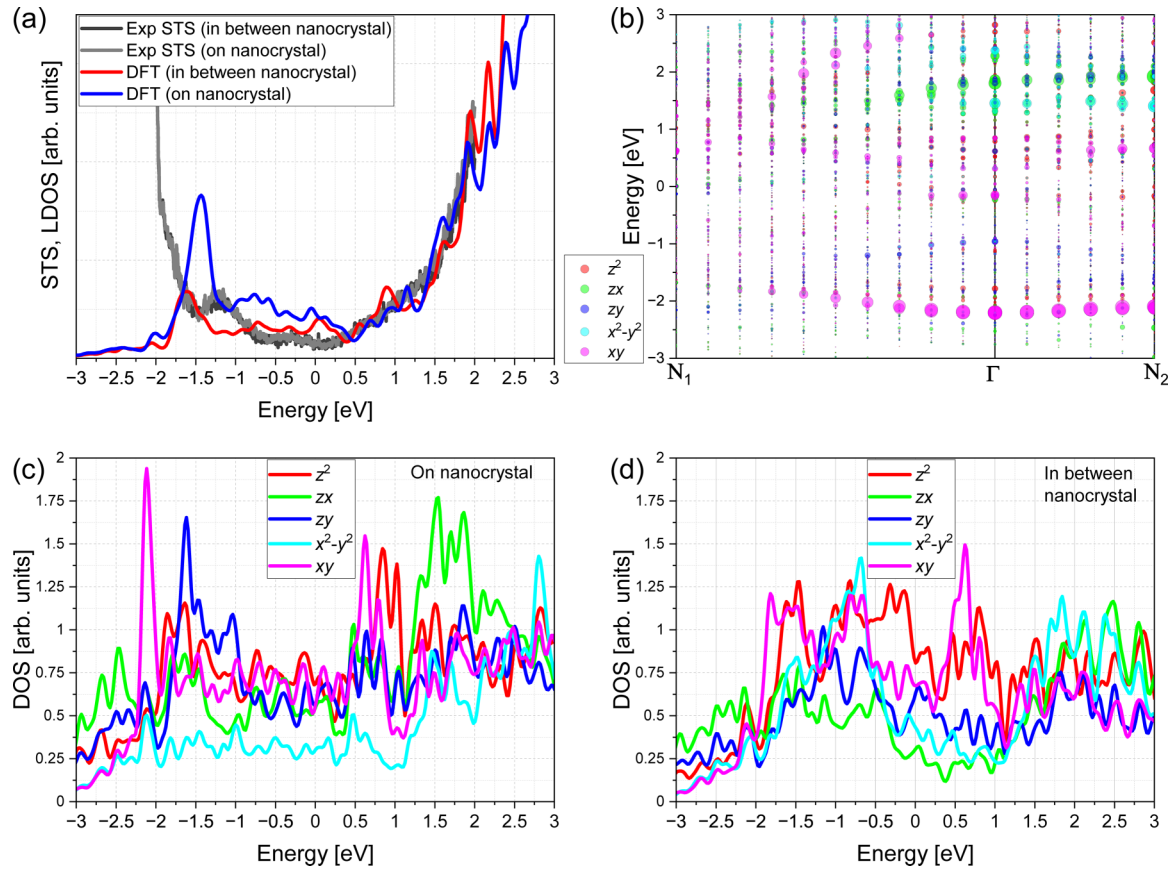
FIG. 3. (a) Simulated LDOS at a distance 4 Å above the surface, compared with measured experimental STS spectrum. (b) m_l projected band structure for the surface nanocrystal atoms; (c),(d) m_l resolved DOS on and between the nanocrystal.

exist mostly around -2.2 eV and have an xy orbital character. As expected, we do not see any resonance at -2.2 eV coming from these states in the theoretical STS [Fig. 3(a)] due to the orientation of the xy orbitals, where the majority of electron density lies in the plane. We can understand the origin of the peak at -1.5 eV in the theoretical STS by looking at the m_l projected density of states for the surface atoms on and between the nanocrystals [Figs. 3(c) and 3(d), respectively]. We see that around -1.5 eV, both contain a significant z^2 component, but on the nanocrystal, there is a significant peak of zy character, which is missing for the atoms between the nanocrystal. For these atoms between the nanocrystal, the in plane xy orbitals play a more significant role. Therefore, we assign the resonance at -1.5 V observed in the theoretical STS to these zy states. We note that this does not point to a zy surface state; as can be seen from the band structure, no such heavily localized state exists. The states responsible for this peak are bulklike, but with a high enough density to cause the peak in the calculated STS. The combination of the bulklike nature of these states, and the tip states dominating the tunneling process in this regime, cause this feature to be unseen in the experimental STS. Overall, we see strong agreement between the DFT calculations and STM/STS experiments for this model.

C. Global electronic structure

One of the most intriguing parts of this surface reconstruction is the measured core level binding energies. Despite the

Nb/O ratio being close to 1 [9,28], the Nb $3d$ level shows an anomalous binding energy of 203.55 eV, a change in binding energy (ΔB.E.) of 1.55 eV relative to the bulk [26,33]. This does not match up with any of the known bulk niobium oxides. We calculate a change in binding energy for the surface Nb atoms of 1.43 eV relative to the bulk, in good agreement with the experimentally determined change. For the O $1s$ level, two different chemical states O_I and O_{II} are observed with energies 530.3 eV and 531.8 eV, ΔB.E. of 1.5 eV with respect to one another [26,33]. The latter binding energy (531.8 eV) matches up exactly with the O $1s$ binding energy in bulk NbO, while the former (530.3 eV) does not match with any bulk niobium oxide. Within this oxygen monolayer model, the two chemical states are the threefold oxygen and the fourfold oxygen in Figs. 1(c) and 1(f). For this change in binding energy, we calculate a value of 1.63 eV, again in good agreement with the experimental value. Because the exact ratio between the two chemical states of oxygen varies significantly between studies, we cannot compare this directly to the DFT calculations. However, in all studies there is always an asymmetry between the two chemical states, the O_I chemical state is always more abundant than the O_{II} chemical state. This agrees with the oxygen monolayer model presented here, where the threefold oxygens correspond to O_I and the fourfold oxygens correspond to O_{II}. Additionally, the O_{II} oxygen is slightly deeper into the surface [see side view in Fig. 1(f)]. This accounts for the angle resolved XPS of Razinkin *et al.* [33], where they observe a higher O_I/O_{II} ratio at glancing angle

TABLE I. Comparison of simulated and experimental core level binding energies and work function.

	Calculated	Experimental
Nb $3d$ ΔB.E. (eV)	1.43 (this work)	1.55 [26,33]
O $1s$ ΔB.E. (eV)	1.63 (this work)	1.50 [26,33]
Work function ϕ (eV)	5.2 (this work)	5.0 (this work)
$h\nu - \phi$ (eV)	16.0 (this work)	16.2 (this work)

compared to normal incidence. Table I shows the comparison between the experimentally fitted change in binding energy and the calculated values. Overall, there is strong agreement between XPS experiments and the oxygen monolayer model.

Looking now at the valence band XPS, we start by comparing the calculated DOS for the infinite nanocrystal model Fig. 4(a) to the experimentally measured XPS. We can see broadly good agreement between the two curves; however, the peaks in the vicinity of −5 eV give rise to a higher intensity than that observed in the experiment. In order to improve agreement between the valence band XPS and calculated DOS, we must account for the finite nature of the crystal by including the channels separating the nanocrystals [Fig. 4(b)]. The finite nanocrystal including the channels drastically improves agreement between the simulated DOS and measured valence band XPS. The behavior of the DOS around −5 eV

is now fully captured and agreement near the Fermi level remains strong. From the orbital resolved DOS in Figs. 4(a) and 4(b) we see that the main broad peak from 0 to −5 eV arises from mostly Nb $4d$ states, whereas the shoulder around −5 to −7 eV comes mostly from the O $2p$. The deep feature around −18 eV is almost entirely arising from semicore O $2s$ states.

Overall, it is not surprising that, to obtain the correct DOS, the finite nature of the pattern must be included. While simulated STM images are highly local, and depend mostly on the local charge density on a surface atom, the total DOS will be highly sensitive to the total band structure across the entire Brillouin zone. When moving to the finite model the band structure will change dramatically, with the bcc[−111]/fcc[0 − 11] direction in the Brillouin zone (along the nanocrystals) shrinking by as much as a factor of $\simeq 10$. Therefore, a significant change in parts of the DOS is to be expected. It is also worth noting that since the channels separating the nanocrystals appear disordered in STM, simulating it using periodic DFT poses a challenge. For the purpose of ruling out the effect of the channel structure on the DOS we evaluate the three possible extremes of the channel structure. Figure 4(c) shows the three structures of finite nanocrystals considered, with different atomic structures in the channels, i.e., no oxygen/niobium in the channel (i.e., a step edge) (type 1), partial oxygen but no niobium (type 2), and partial oxygen/partial niobium (type 3). Figure 4(d) shows the
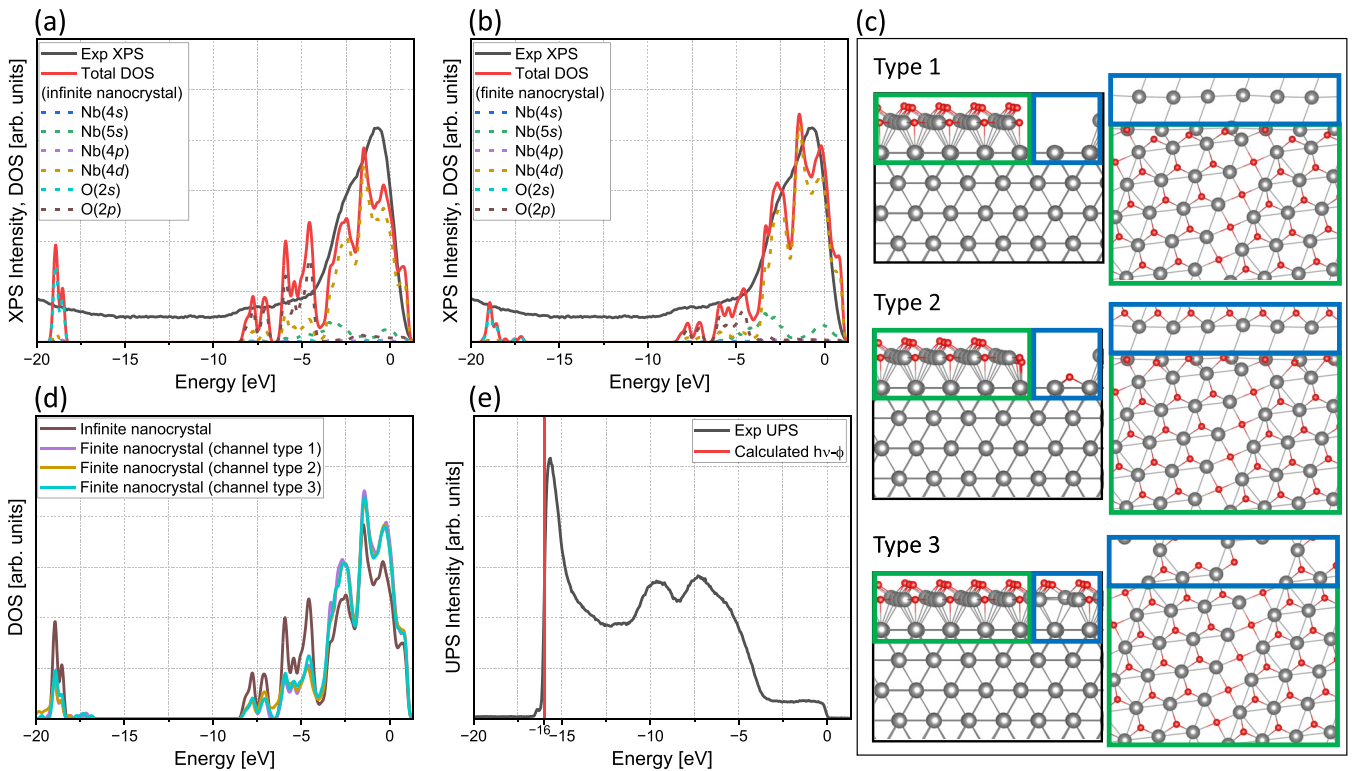

FIG. 4. (a),(b) Simulated total DOS over the whole slab with orbital decomposition, compared against measured valence band XPS for infinite and finite nanocrystals, respectively. (c) Side and top views for the three different channel structures considered here, with the channel area highlighted by the blue rectangles and the nanocrystal area highlighted by the green rectangles. (d) Total DOS calculated for the three finite nanocrystal structures compared to infinite nanocrystal. (e) Experimental UPS spectrum compared with calculated value for the secondary electron cutoff $h\nu - \phi$.

calculated DOS for these three structures compared to the infinite nanocrystal. We can see that, while there is a clear difference between the infinite nanocrystal calculation (no channel) and the calculations including the channels, there is little difference between the calculated DOS for the different types of channel structures.

From our UPS experiment [Fig. 4(e)], the work function (ϕ) of this surface can be obtained by comparing the incident photon energy to the secondary electron cutoff ($E_{sec} = h\nu - \phi$). Using this method we obtain a work function of 5.0 eV (Table I). Comparing this result with the work function of Nb metal (4.3 eV) and Nb_2O_5 (5.2 eV) [62], we see the expected trend is upheld, with the work function increasing as more oxygen is added. Within DFT we can estimate the work function by comparing the classical electric potential at a point far from the surface slab with the Fermi level. From this method we obtain a calculated work function of 5.2 eV, showing decent agreement with the experimentally measured value.

IV. CONCLUSIONS

From the above discussion, it seems clear that the oxygen monolayer surface is the best candidate for explaining the surface reconstruction. Due to the unusual structure of this surface, it is worth discussing how correct it is to call this surface structure a NbO structure. While the stoichiometry of the surface measured from XPS suggests the ratio of oxygen and niobium to be very close to 1, the anomalous Nb $3d$ core level binding energy suggests that the chemical environment of these atoms is not similar to that of bulk NbO. Our model confirms this, with none of the niobium atoms being square planar coordinated (as they are in bulk NbO). Some papers have discussed this anomalous binding energy in terms of a suboxide Nb_2O [63–65]. However, in these studies, the atoms

assigned to that suboxide are buried underneath a Nb_2O_5 layer and as previously mentioned the stoichiometry contradicts this suboxide interpretation. The crystallography also suggests that this layer is not simply a NbO monolayer. This surface therefore appears to be a novel 2D niobium oxide layer, with no bulk counterpart.

Having determined the precise local structure of this oxide layer, there is now a foundation in place upon which effect of the niobium surface structure on device performance can be understood. This surface structure will be present on any Nb(110) facet, either buried underneath higher valence oxides or on its own. In the case of SRF cavities specifically, this surface structure may be the dominant surface oxide present in samples showing improved performance after vacuum annealing [22]. Whatever the mechanism for the improvement in device performance may be, it is likely that this surface structure plays a significant role.

[1] P. Kneisel, G. Ciovati, P. Dhakal, K. Saito, W. Singer, X. Singer, and G. Myneni, Nucl. Instrum. Methods Phys. Res., A **774**, 133 (2015).

[2] M. Wenskat, J. Čižek, M. O. Liedke, M. Butterling, C. Bate, P. Haušild, E. Hirschmann, A. Wagner, and H. Weise, Sci. Rep. **10**, 8300 (2020).

[3] M. Wenskat, J. Čižek, M. O. Liedke, M. Butterling, M. Stiehl, G. D. L. Semione, C. Backes, C. Bate, O. Melikhova, E. Hirschmann, A. Wagner, H. Weise, A. Stierle, M. Aeschlimann, and W. Hillert, Phys. Rev. B **106**, 094516 (2022).

[4] P. J. Leek, S. Filipp, P. Maurer, M. Baur, R. Bianchetti, J. M. Fink, M. Göppl, L. Steffen, and A. Wallraff, Phys. Rev. B **79**, 180511(R) (2009).

[5] W. D. Oliver, Y. Yu, J. C. Lee, K. K. Berggren, L. S. Levitov, and T. P. Orlando, Science **310**, 1653 (2005).

[6] Y. Asada and H. Nosé, J. Phys. Soc. Jpn. **26**, 347 (1969).

[7] G. Ciovati, Appl. Phys. Lett. **89**, 022507 (2006).

[8] M. Delheusy, A. Stierle, N. Kasper, R. P. Kurta, A. Vlad, H. Dosch, C. Antoine, A. Resta, E. Lundgren, and J. Andersen, Appl. Phys. Lett. **92**, 101911 (2008).

[9] C. Sürgers, M. Schöck, and H. V. Löhneysen, Surf. Sci. **471**, 209 (2001).

[10] C. C. Koch, J. O. Scarbrough, and D. M. Kroeger, Phys. Rev. B **9**, 888 (1974).

[11] A. Odobesko, F. Friedrich, S.-B. Zhang, S. Haldar, S. Heinze, B. Trauzettel, and M. Bode, Phys. Rev. B **102**, 174502 (2020).

[12] R. D. Veit, N. A. Kautz, R. G. Farber, and S. Sibener, Surf. Sci. **688**, 63 (2019).

[13] S. L. Prischepa, V. N. Kushnir, C. Cirillo, V. Granata, I. Komissarov, N. G. Kovalchuk, M. M. Mikhalik, A. L. Danilyuk, I. A. Svito, M. Andrulevicius, and C. Attanasio, Supercond. Sci. Technol. **34**, 115021 (2021).

[14] T. F. Harrelson, E. Sheridan, E. Kennedy, J. Vinson, A. T. N'Diaye, M. V. P. Altoé, A. Schwartzberg, I. Siddiqi, D. F. Ogletree, M. C. Scott, and S. M. Griffin, Appl. Phys. Lett. **119**, 244004 (2021).

[15] N. P. de Leon, K. M. Itoh, D. Kim, K. K. Mehta, T. E. Northup, H. Paik, B. S. Palmer, N. Samarth, S. Sangtawesin, and D. W. Steuerman, Science **372**, eabb2823 (2021).

[16] A. Premkumar, C. Weiland, S. Hwang, B. Jäck, A. P. M. Place, I. Waluyo, A. Hunt, V. Bisogni, J. Pelliciari, A. Barbour, M. S.

Miller, P. Russo, F. Camino, K. Kisslinger, X. Tong, M. S. Hybertsen, A. A. Houck, and I. Jarrige, Commun. Mater. **2**, 72 (2021).

[17] A. Romanenko and D. I. Schuster, Phys. Rev. Lett. **119**, 264801 (2017).

[18] C. D. L. Semione, V. Vonk, A. D. Pandey, E. Grånäs, B. Arndt, M. Wenskat, W. Hillert, H. Noei, and A. Stierle, J. Phys.: Condens. Matter **33**, 265001 (2021).

[19] A. Prudnikava, Y. Tamashevich, S. Babenkov, A. Makarova, D. Smirnov, V. Aristov, O. Molodtsova, O. Kugeler, J. Viefhaus, and B. Foster, Supercond. Sci. Technol. **35**, 065019 (2022).

[20] Y. Trenikhina, A. Romanenko, J. Kwon, J.-M. Zuo, and J. F. Zasadzinski, J. Appl. Phys. **117**, 154507 (2015).

[21] J. Verjauw, A. Potočnik, M. Mongillo, R. Acharya, F. Mohiyaddin, G. Simion, A. Pacco, T. Ivanov, D. Wan, A. Vanleenhove, L. Souriau, J. Jussot, A. Thiam, J. Swerts, X. Piao, S. Couet, M. Heyns, B. Govoreanu, and I. Radu, Phys. Rev. Appl. **16**, 014018 (2021).

[22] G. Ciovati, G. Myneni, F. Stevie, P. Maheshwari, and D. Griffis, Phys. Rev. ST Accel. Beams **13**, 022002 (2010).

[23] RF superconductivity, in *Proceedings, 8th Workshop, Abano Terme, Padua, Italy, October 610, 1997*, Vol. 1: Superconducting particle accelerators, Vol. 2: Surface resistance and non-accelerator applications, Vol. 3: Resonator construction technologies, Vol. 4: Superconducting materials and thin films, edited by V. Palmieri and A. Lombardi, Vol. 60 (Gordon and Breach, Amsterdam, Netherlands, 1998), pp. 1–264.

[24] A. Gurevich, Rev. Accel. Sci. Technol. **05**, 119 (2012).

[25] A. Gurevich and G. Ciovati, Phys. Rev. B **77**, 104501 (2008).

[26] K. Zhussupbekov, K. Walshe, S. I. Bozhko, A. Ionov, K. Fleischer, E. Norton, A. Zhussupbekova, V. Semenov, I. V. Shvets, and B. Walls, Sci. Rep. **10**, 3794 (2020).

[27] A. S. Razinkin and M. V. Kuznetsov, Phys. Met. Metallogr. **110**, 531 (2010).

[28] I. Arfaoui, J. Cousty, and H. Safa, Phys. Rev. B **65**, 115413 (2002).

[29] A. Yazdani, B. A. Jones, C. P. Lutz, M. F. Crommie, and D. M. Eigler, Science **275**, 1767 (1997).

[30] O. Hellwig and H. Zabel, Phys. B: Condens. Matter **336**, 90 (2003).

[31] M. Delheusy, Ph.D. thesis, Paris-Sud University, 2008.

[32] Z. P. Hu, Y. P. Li, M. R. Ji, and J. X. Wu, Solid State Commun. **71**, 849 (1989).

[33] A. S. Razinkin, E. V. Shalaeva, and M. V. Kuznetsov, Phys. Met. Metallogr. **106**, 56 (2008).

[34] A. B. Odobesko, S. Haldar, S. Wilfert, J. Hagen, J. Jung, N. Schmidt, P. Sessi, M. Vogt, S. Heinze, and M. Bode, Phys. Rev. B **99**, 115437 (2019).

[35] R. Boshuis, A. Odobesko, F. Friedrich, J. Jung, and M. Bode, Phys. Rev. Mater. **5**, 054801 (2021).

[36] P. Beck, L. Schneider, L. Rózsa, K. Palotás, A. Lászlóffy, L. Szunyogh, J. Wiebe, and R. Wiesendanger, Nat. Commun. **12**, 2040 (2021).

[37] P. Beck, L. Schneider, L. Bachmann, J. Wiebe, and R. Wiesendanger, Phys. Rev. Mater. **6**, 024801 (2022).

[38] C. E. Lekka, M. J. Mehl, N. Bernstein, and D. A. Papaconstantopoulos, Phys. Rev. B **68**, 035422 (2003).

[39] D. Kilimis and C. Lekka, Mater. Sci. Eng., B **144**, 27 (2007).

[40] Q.-G. Wang and J.-X. Shang, J. Phys.: Condens. Matter **24**, 225005 (2012).

[41] D. N. Tafen and M. C. Gao, JOM **65**, 1473 (2013).

[42] See Supplemental Material at http://link.aps.org/supplemental/10.1103/PhysRevB.107.165425 for simulations of models previously presented in the literature, which also contains Refs. [43–45].

[43] A. K. Efimenko, N. Hollmann, K. Hoefer, J. Weinen, D. Takegami, K. K. Wolff, S. G. Altendorf, Z. Hu, A. D. Rata, A. C. Komarek, A. A. Nugroho, Y. F. Liao, K.-D. Tsuei, H. H. Hsieh, H.-J. Lin, C. T. Chen, L. H. Tjeng, and D. Kasinathan, Phys. Rev. B **96**, 195112 (2017).

[44] Z. Hu, G. Qian, S. Li, L. Yang, X. Chen, M. Weng, W. Tan, and F. Pan, Sci. Bull. **65**, 367 (2020).

[45] W. W. Schulz and R. M. Wentzcovitch, Phys. Rev. B **48**, 16986 (1993).

[46] I. Arfaoui, J. Cousty, and C. Guillot, Surf. Sci. **557**, 119 (2004).

[47] P. Giannozzi, O. Baseggio, P. Bonfà, D. Brunato, R. Car, I. Carnimeo, C. Cavazzoni, S. De Gironcoli, P. Delugas, F. Ferrari Ruffino, A. Ferretti, N. Marzari, I. Timrov, A. Urru, and S. Baroni, J. Chem. Phys. **152**, 154105 (2020).

[48] P. Giannozzi, S. Baroni, N. Bonini, M. Calandra, R. Car, C. Cavazzoni, D. Ceresoli, G. L. Chiarotti, M. Cococcioni, I. Dabo, A. D. Corso, S. de Gironcoli, S. Fabris, G. Fratesi, R. Gebauer, U. Gerstmann, C. Gougoussis, A. Kokalj, M. Lazzeri, L. Martin-Samos *et al.*, J. Phys.: Condens. Matter **21**, 395502 (2009).

[49] J. P. Perdew, K. Burke, and M. Ernzerhof, Phys. Rev. Lett. **77**, 3865 (1996).

[50] A. Dal Corso, Comput. Mater. Sci. **95**, 337 (2014).

[51] N. Marzari, D. Vanderbilt, A. De Vita, and M. C. Payne, Phys. Rev. Lett. **82**, 3296 (1999).

[52] K. Momma and F. Izumi, J. Appl. Crystallogr. **44**, 1272 (2011).

[53] J. Tersoff and D. R. Hamann, Phys. Rev. Lett. **50**, 1998 (1983).

[54] J. Tersoff and D. R. Hamann, Phys. Rev. B **31**, 805 (1985).

[55] K. Zhussupbekov, K. Walshe, B. Walls, A. Ionov, S. I. Bozhko, A. Ksenz, R. N. Mozhchil, A. Zhussupbekova, K. Fleischer, S. Berman, I. Zhilyaev, D. D. O'Regan, and I. V. Shvets, J. Phys. Chem. C **125**, 5549 (2021).

[56] D. V. Potorochin, A. N. Chaika, O. V. Molodtsova, V. Y. Aristov, D. E. Marchenko, D. A. Smirnov, A. A. Makarova, B. Walls, K. Zhussupbekov, K. Walshe, I. V. Shvets, A. S. Ciobanu, M. K. Rabchinskii, N. V. Ulin, M. V. Baidakova, P. N. Brunkov, and S. L. Molodtsov, Appl. Surf. Sci. **585**, 152542 (2022).

[57] A. S. Frolov, J. Sánchez-Barriga, C. Callaert, J. Hadermann, A. V. Fedorov, D. Y. Usachov, A. N. Chaika, B. C. Walls, K. Zhussupbekov, I. V. Shvets, M. Muntwiler, M. Amati, L. Gregoratti, A. Y. Varykhalov, O. Rader, and L. V. Yashina, ACS Nano **14**, 16576 (2020).

[58] L. V. Yashina, T. S. Zyubina, R. Püttner, A. S. Zyubin, V. I. Shtanov, and E. V. Tikhonov, J. Phys. Chem. C **112**, 19995 (2008).

[59] S. De Waele, K. Lejaeghere, M. Sluydts, and S. Cottenier, Phys. Rev. B **94**, 235418 (2016).

[60] K. Zhussupbekov, C. P. Cullen, A. Zhussupbekova, I. V. Shvets, G. S. Duesberg, N. McEvoy, and C. Ó. Coileáin, RSC Adv. **10**, 42001 (2020).

[61] K. Zhussupbekov, L. Ansari, J. B. McManus, A. Zhussupbekova, I. V. Shvets, G. S. Duesberg, P. K. Hurley, F. Gity, C. Ó. Coileáin, and N. McEvoy, npj 2D Mater. Appl. **5**, 14 (2021).

[62] P. V. Tyagi, M. Doleans, B. Hannah, R. Afanador, C. McMahan, S. Stewart, J. Mammosser, M. Howell, J. Saunders, B. Degraff, and S. H. Kim, Appl. Surf. Sci. **369**, 29 (2016).

[63] Q. Ma and R. A. Rosenberg, Appl. Surf. Sci. **206**, 209 (2003).

[64] Q. Ma, P. Ryan, J. W. Freeland, and R. A. Rosenberg, J. Appl. Phys. **96**, 7675 (2004).

[65] J. Sebastian, D. Seidman, K. Yoon, P. Bauer, T. Reid, C. Boffo, and J. Norem, Phys. C: Supercond. **441**, 70 (2006).